

# Optimizing the conductivity, microstructure and mechanical properties of tape-cast LATP with LiF and SiO<sub>2</sub> additives

Jürgen Peter Gross (✉ [j.gross@fz-juelich.de](mailto:j.gross@fz-juelich.de))

Forschungszentrum Jülich <https://orcid.org/0000-0001-5325-9874>

Jürgen Malzbender

Forschungszentrum Jülich: Forschungszentrum Julich GmbH

Enkhtsetseg Dashjav

Forschungszentrum Jülich: Forschungszentrum Julich GmbH

Frank Tietz

Forschungszentrum Jülich GmbH: Forschungszentrum Julich GmbH

Ruth Schwaiger

Forschungszentrum Jülich: Forschungszentrum Julich GmbH

---

## Research Article

**Keywords:** Solid state battery, LATP, solid electrolytes, tape-casting, conductivity, mechanical properties

**Posted Date:** August 24th, 2021

**DOI:** <https://doi.org/10.21203/rs.3.rs-829169/v1>

**License:**   This work is licensed under a Creative Commons Attribution 4.0 International License.

[Read Full License](#)

---

# Abstract

LATP sheets with LiF and SiO<sub>2</sub> addition prepared by tape casting as electrolytes for solid-state batteries were characterized regarding conductivity, microstructure and mechanical properties aiming towards an optimized composition. The use of additives permitted a lowering of the sintering temperature. As general trend, higher LiF to SiO<sub>2</sub> ratios led to lower porosities. This decrease in the porosity corresponds to an increase of the ionic conductivity as well as higher values of elastic modulus and hardness determined by indentation testing. Micro-pillar testing was used to assess the crack growth behavior, revealing weak grain boundaries.

## 1 Introduction

Batteries are considered a key technology for the transportation sector and storage of renewable energy [1]. Therefore, in recent years, a large number of studies has concentrated on the development of next generation battery technologies. They focused mainly on two aspects: the optimization of current batteries and the development of new materials for next-generation batteries, especially all-solid-state batteries [2], where in particular materials possessing the NaSICON (Na<sup>+</sup> Super Ionic CONductors) structure are considered to be promising solid electrolytes [3, 4].

In particular, for the application in all-solid-state lithium batteries, Li<sub>1+x</sub>Al<sub>x</sub>Ti<sub>2-x</sub>(PO<sub>4</sub>)<sub>3</sub> (LATP) with the NaSICON structure, is a favorable material due to high ionic conductivity [5]. However, issues related to crack formation or delamination of interfaces can deteriorate material properties and battery performance [1]. In fact, a large number of publications are available on different synthesis approaches and resulting conductivities of LATP [6–15], but only a limited number of publications have addressed the failure-relevant mechanical properties of solid electrolytes [6, 16–20].

In general, to warrant reliable operation, ceramic materials should not change properties due to operation, deform only elastically and be resistant to crack growth [21]. Hence, especially the characterization of the elastic modulus and the crack growth behavior is important. Additional challenges arise for tape-cast solid electrolytes. This processing route promises to fulfil requirements for large-scale fabrication, reduced costs and thin separators [22], but complicates the determination of mechanical properties due to the limited thickness [23], in particular for the fracture toughness  $K_{IC}$ , which is based frequently on the Vickers indentation testing [24]. However, Sebastiani et al. [24, 25] established a micro-pillar indentation splitting method that can facilitate the determination of the local fracture toughness. This method was already successfully used to derive the intragranular fracture toughness of LATP by testing micro-pillars prepared within large grains [20]. In order to determine the resistance of the solid electrolyte against lithium dendrite formation and growth, though, potential effects of intergranular and transgranular crack growth on the fracture toughness must also be considered [1].

In this work, the influence of LiF and SiO<sub>2</sub> additives on the apparent ionic conductivity, on the microstructure and the mechanical properties of LATP was studied. Pure and sample with LiF as well as

SiO<sub>2</sub> additives were prepared by tape casting. The ionic conductivity was measured by impedance spectroscopy and the microstructure was analyzed using scanning electron microscopy. Elastic modulus and hardness of the specimens were characterized using different indentation methods. The fracture toughness was estimated from the splitting of focused ion beam (FIB) fabricated micro-pillars.

## 2 Experimental

A solution-assisted solid state reaction was used to prepare LATP powder as described in detail elsewhere [26, 27]. Subsequently, the powder was calcined at 700°C for 4 h. The resulting material was ball-milled for 24 h in ethanol using ZrO<sub>2</sub> balls, then dried for 24 h at 70°C and mortared. The particle size distribution in ethanol suspension was measured by laser scattering analysis (Horiba LA 950 V2) using the Fraunhofer scattering approximation [28]. The specific surface area was measured according to the Brunauer-Emmett-Teller (BET) method with nitrogen gas. The obtained powder had a mean particle size, D<sub>50</sub>, of 0.78 μm and a specific surface area of 15.23 m<sup>2</sup> g<sup>-1</sup>. It was then dispersed in a mixture of ethanol, methyl-ethyl-ketone, polyvinylbutyral (Butvar B-98), Nousperse FX9086 (Elementis Specialties), polyethylene glycol (PEG400), and Solusolv S-2075 (Solutia Inc.) and sintering additives of an amorphous SiO<sub>2</sub> (Alfa Aesar) and LiF (Alfa Aesar).

In a previous work [29], 1.5 % of an amorphous SiO<sub>2</sub> nano-powder (Alfa Aesar) was used as sintering additive to improve conductivity and mechanical properties of electrolyte sheets. Here, different ratios of SiO<sub>2</sub> and LiF varying from 1:1.5 to 1:4 (summarized in Table 1) were used to improve sinterability, ionic conductivity and mechanical properties.

Table 1  
Targeted compositions of the samples.

Sample	LiF - addition [wt.-%]	SiO <sub>2</sub> - addition [wt.-%]	Ratio
LATP:Pure	0.0	0.0	-
LATP:1.5F0.5Si	1.5	0.5	3:1
LATP:1.5F1Si	1.5	1.0	1.5:1
LATP:2F0.5Si	2.0	0.5	4:1

The slurry was homogenized and polymerized for 48 h and then degassed at 20 kPa for 10 minutes before tape casting in a micro-tape caster (KARO Cast 300-7, KMS-Automation GmbH, Germany). A slit height of 350 μm and a drawing speed of 3.5 mm/s were used. The cast foils were dried and cut into circular discs of 16 mm in diameter. These discs were then sintered in air at different temperatures for 4 h, resulting in 90–110 μm thick sheets.

In order to choose an optimal sintering temperature, the sintering behavior of the tape-cast green sheets was analyzed by dilatometry (DIL 402C, Netzsch). The sintered disks were then analyzed by means of X-ray diffraction analysis (XRD) using an EMPYREAN diffractometer (PANalytical), with a Cu-LFF-tube operated at 40 kV and 40 mA. The measurement was conducted in the  $2\theta$ -range of  $5^\circ$  to  $90^\circ$ , with a step size of  $0.026^\circ$  and a dwell time per step of 2 s. The resulting XRD patterns were analyzed by Rietveld refinement using the software TOPAS (Bruker AXS).

In order to measure the ionic conductivity, the surfaces were sputtered with gold on both sides and placed into an electrochemical cell (EL-CELL, PAT-Cell) under Ar atmosphere. The impedance spectra were measured using a potentiostat (Bio-Logic, SP-300) in the frequency range of 7 MHz to 1 Hz.

The samples were embedded in water-free epoxy resin and manually polished using 400 to 4000 SiC grinding papers, for the subsequent microstructural and mechanical characterization. The fine-polishing was conducted with a Minimet® 100 polisher using water-free diamond suspensions with grain sizes from of  $4\ \mu\text{m}$  down to  $1\ \mu\text{m}$ . The final polishing was conducted using water-free colloidal silica polishing solution with a grain size of  $0.2\ \mu\text{m}$ . For LAMP, the water-free sample preparation was necessary to prevent a reaction with water [30, 31]. Scanning electron microscopy (SEM) images were obtained using a Zeiss Merlin SEM (Carl Zeiss Microscopy, Oberkochen, Germany). The porosity was estimated based on the analysis of SEM micrographs using ImageJ [32]. At least six SEM images were obtained and analyzed for each sample.

Elastic moduli  $E$  and hardness values  $H$  were determined from indents into the surface of the embedded and polished samples using a FISCHERSCOPE® HC 100 instrument (Helmut Fischer GmbH, Sindelfingen) equipped with a Vickers diamond tip. The samples were indented to a load of 30 mN to measure the average intrinsic properties of the materials [30]. On each specimen at least 100 indentations were performed with a load application time of 15 s and a hold period of 1 s before unloading the sample. The values of  $E$  and  $H$  were determined from the unloading slope of the load-displacement curve following the DIN EN ISO 3452-1 standard. A Poisson ratio of 0.25 was assumed for all materials [16]. In addition, some indentations were carried out at higher loads using a CSM indenter (Anton Paar CSM Micro-Indentation Tester, Peseux, Switzerland) to test the feasibility of measuring the indentation fracture toughness with a Vickers tip, loads of 50, 300 and 500 mN with loading rates of 30 N/h were applied.

A micro-pillar splitting method was used to estimate effects of intergranular and transgranular crack growth on the fracture toughness of LAMP. Micro-pillars were fabricated by focused ion beam (FIB) cutting using an Auriga cross-beam instrument (Carl Zeiss Microscopy, Oberkochen, Germany) operated at an acceleration voltage and beam currents of 30 kV and 2–16 nA, respectively. In order to minimize any potential influence of FIB damage on  $K_{IC}$ , the diameter of the pillars should be  $10\ \mu\text{m}$  or larger [33]. Therefore, for each specimen 5 pillars with a target diameter of  $10\ \mu\text{m}$  were cut. For the pillar-splitting test, a ratio of  $z/D \sim 1$  is required [24], where  $D$  is the diameter and  $z$  the height of the pillar. Hence in the current work, pillars with  $10\ \mu\text{m}$  in diameter and  $10\ \mu\text{m}$  in height were tested.

For each pillar, topographic images were recorded in order to confirm the pillar geometry using a laser confocal LEXT OLS6000 microscopy instrument (OLYMPUS, Hamburg, Germany) employing a step size of 0.2  $\mu\text{m}$ . The positioning of the indenter tip in the center of the pillars was ensured and errors due to indenter positioning can be neglected [33]. Subsequently load-controlled indentation tests were performed at a load rate of 0.5 mN/s to split the pillars using a NanoXtrem nanoindenter (Micro Materials, Wrexham, UK) equipped with a Berkovich type diamond tip.

### 3 Results And Discussion

Although the amount of sintering additives was  $\leq 3$  wt.-% in all cases, the sintering behavior of LAMP samples was strongly affected by the additives. Figure 1 presents the sintering behavior in terms of the measured shrinkage of the samples from room temperature to 950°C at a constant heating rate of 300 K/h. The two samples with 1.5 % LiF and different amounts of  $\text{SiO}_2$  exhibited very similar shrinkage curves compared to the sample with 2 % LiF. The shrinkage at 815°C for the samples LAMP:1.5F0.5Si and LAMP:1.5F1Si was 24 % and 26 %, respectively (see Fig. 1). Below 700°C no dimensional change could be observed.

According to the dilatometer curves, the LAMP sample without sintering additive started to shrink slowly at around 800°C and reached 22 % shrinkage at 950°C. For the samples with additives, the onset points of shrinkage decreased towards 750°C followed by a sharp increase in shrinkage rate to reach a maximum shrinkage at around 880°C. This corresponded to an almost 130°C reduction of the sintering temperature compared to pure LAMP. In the case of the LAMP:2F0.5Si sample, the onset of the sintering was similar to that of the others, however, the total shrinkage was lower (approximately 20 %). The length expansion at temperatures above 850°C of the three samples containing LiF and  $\text{SiO}_2$  is caused by the melting [34] and slowly increasing evaporation rate of LiF.

As shown earlier [29], single-phase LAMP can be obtained at sintering temperatures above 900°C. In the current work, single-phase LAMP could be obtained without additives via sintering at 940°C, in agreement with the previous work. For the samples with additives the sintering temperature could be reduced to 815°C. In the as-sintered state, the LAMP samples with additives contained  $\text{LiTiOPO}_4$  and  $\text{AlPO}_4$  as secondary phases in low amounts, see Fig. 2 (< 5 wt. % by XRD). Rietveld analysis yielded the same lattice parameters for all LAMP samples.

The total conductivities of the samples are listed in Table 2, along with sintering temperature, sample thickness and corresponding porosity. The sample LAMP:1.5LiF1Si showed the highest ionic conductivity of 0.096 mS/cm, which is similar to the conductivity reported for LAMP with 2 wt.%  $\text{SiO}_2$  [29].

Representative SEM images are shown in Fig. 3. The addition of  $\text{SiO}_2$  and LiF led to a reduced porosity and a more homogenous distribution of the pores than for the pure LAMP sample (Fig. 3a). Although grain boundaries could not be identified, the grain size was probably smaller than the distance between the pores, thus, below 2  $\mu\text{m}$ .

Table 2  
Sintering temperature  $T_{\text{sint}}$ , thickness  $t$ , ionic conductivity  $\alpha_{\text{total}}$   
and porosity.

Sample name	$T_{\text{sint}}$ [°C]	$t$ [ $\mu\text{m}$ ]	$\alpha_{\text{total}}$ [mS/cm]	Porosity [%]-
LATP:Pure	940	110	0.043	$14.7 \pm 2.5$
LATP:1.5F0.5Si	815	90	0.095	$8.7 \pm 0.9$
LATP:1.5F1Si	815	100	0.096	$7.3 \pm 1.0$
LATP:2F0.5Si	820	100	0.083	$5.8 \pm 0.4$

The porosity decreased for the specimens with LiF and SiO<sub>2</sub> additives compared to the pure LATP. The additives reduced the porosity from  $14.7 \pm 2.5\%$  for the pure LATP to  $5.8 \pm 0.4\%$  for the LATP specimens with an addition of 2 wt.-% LiF and 0.5 wt.-% SiO<sub>2</sub>. The pore size of  $\sim 0.5 \pm 0.3 \mu\text{m}$  is the same for all specimens independent of the sintering additives.

As the additives appear not to be incorporated in the crystal structure of LATP, the same hardness and elastic behavior might be expected. However, as illustrated in Fig. 4 (a) and (b), the SiO<sub>2</sub> as well as the LiF addition seem to enhance elastic moduli and hardness values. For pure LATP, elastic moduli ranging from 81 to 115 GPa have been reported [35], whereas the average value for pure LATP obtained in this work is  $64 \pm 5$  GPa and, thus, significantly lower. The elastic moduli of the specimens with LiF and SiO<sub>2</sub> addition are between  $\sim 94$  and  $\sim 106$  GPa and therefore well within the range reported for pure LATP. The hardness value reported in the literature for pure LATP is  $7.1 \pm 1.0$  GPa [35]. However, here pure LATP revealed a much lower hardness of  $2.9 \pm 0.6$  GPa, while for the material with LiF and SiO<sub>2</sub> addition the hardness values vary between  $\sim 8.4$  and  $\sim 11.4$  GPa.

As mentioned above, the additives have a significant effect on the porosity, which needs to be considered in the interpretation of the data obtained from the indentation tests. Thus, in Fig. 4 (c) and (d) the elastic modulus and hardness data are presented as a function of the porosity, revealing that both properties are significantly affected by the porosity. The impact of porosity on the elastic modulus of materials is already known and a number of different models have been proposed in order to explain this dependency [36–39].

In order to assess if a derivation of the properties based on the frequently used measurement of radial or Palmqvist type cracks is possible, i.e. to see if the properties obtained for such thin specimens are affected by the low compliance of the embedding material, Vickers indentations were carried out on a LATP:2F0.5Si specimen. The derived elastic modulus and hardness values decreased significantly with increasing load due to the deformation of the embedding material (see supplementary Figure SupplInfo1), thus, ruling out the use of this method.

A typical micro-pillar prior to testing is shown in Fig. 5. The pillar size is much larger than the grain size. Furthermore, the polycrystalline nature of the pillars can clearly be seen. The surface was not perfectly flat due to the porosity and an angle of approximately  $15^\circ$  existed between the side walls and the surface normal, as determined by laser confocal microscopy. In addition the top surface of the pillars was slightly elliptical rather than circular and the edges were slightly rounded. However, such imperfections have also been reported in other studies for FIB-milled micro-pillars and it has been shown that any potential influence on the results decreased with increasing pillar size, i.e. being insignificant for the pillar sizes used in this work [31].

Representative images of the micro-pillars after the indentation testing are shown in Fig. 6. Figure 6 (a) shows a deformed micro-pillar of specimen L ATP:Pure. The indenter tip displaced the grains rather than deforming them due to the high porosity, therefore a clear imprint is not visible. The displacement of the grains led to secondary cracks along the grain boundaries indicating weak grain boundaries. When the load was further increased, beyond the apparent critical load, the micro-pillar rather disintegrated into a pile of individual grains instead of being clearly crushed, as can be seen in Fig. 6 (b). This observation underscores the presence of weak grain boundaries. By contrast, the micro-pillars of the sample L ATP:1.5F0.5Si showed an indentation imprint after testing. The crack origin seems to be located in the vicinity of the corners of the imprints, while small deviations might be explained by pores at the surface of the pillars. Secondary cracks can be observed, although it is unclear whether they were induced during the loading or rather upon unloading of the tip. Again, the cracks seem to propagate along the grain boundaries indicating intergranular fracture. An increase of the load beyond the critical load also leads to disintegration of the micro-pillar, as shown in Fig. 6 (c) and (d). The specimens L ATP:1.5F1Si and L ATP:2F0.5Si behave similarly in the micro-pillar test. For both specimens a crack formed parallel to the edge of the imprint, which seems to originate from pores located at the micro-pillar surface and to propagate along the grain boundaries (Fig. 6 (e) and (f)). This behavior is consistent for all micro-pillars of these two samples. The results clearly show that the grain boundaries need to be improved. Based on the equations given in [24], fracture toughness values can be estimated in the range of  $0.2$  to  $0.4 \text{ MPa m}^{1/2}$ .

## 4 Conclusion

In this work, the influence of LiF and SiO<sub>2</sub> additions on the apparent ionic conductivity, microstructure and mechanical properties of sintered tape-cast L ATP sheets, with thicknesses of around  $\sim 100 \mu\text{m}$ , has been investigated. The use of LiF and SiO<sub>2</sub> additives allowed a reduction of the sintering temperature and a reduction of the porosity. In addition, the ionic conductivity improved compared to pure L ATP due to a reduction of the porosity.

In summary, the highest elastic moduli and hardness values were observed for L ATP:1.5F1Si and L ATP:2F0.5Si. However, the results were significantly affected by the porosity. A further reduction of the porosity of tape-cast L ATP would certainly improve the physical and mechanical properties, which might be achieved by an optimization of the LiF and SiO<sub>2</sub> sintering additives.

A micro-pillar splitting technique was used to investigate the crack growth behavior. It was shown that the grain boundaries need to be improved, since intergranular crack propagation was observed and the micro-pillars disintegrated into individual grains.

## Declarations

## Acknowledgement

The authors thank Dr. E. Wessel and Dr. D. Grüner for the SEM analyses, Mr. M. Ziegner for XRD analyses, Ms. D. Eßer for the FIB preparation and Mr. M. Turiaux for technical support. Financial support from the German Federal Ministry of Education and Research (BMBF) related to the project “ProFeLi” (support code 13XP0184B) is gratefully acknowledged.

## References

1. Famprakis T, Canepa P, Dawson JA, Islam MS, Masquelier C (2019) Fundamentals of inorganic solid-state electrolytes for batteries. *Nat Mater* 18:1278–1291
2. Placke T, Kloepsch R, Dühnen S, Winter M (2017) Lithium ion, lithium metal, and alternative rechargeable battery technologies: the odyssey for high energy density. *J of Solid State Electrochem* 21:1939–1964
3. Goodenough JB, Hong HP, Kafalas J (1976) Fast Na<sup>+</sup>-ion transport in skeleton structures. *Mater Res Bull* 11:203–220
4. Hong HP (1976) Crystal structures and crystal chemistry in the system Na<sub>1+x</sub>Zr<sub>2</sub>Si<sub>x</sub>P<sub>3-x</sub>O<sub>12</sub>. *Mater Res Bull* 11:173–182
5. Fu J (1997) Superionic conductivity of glass-ceramics in the system Li<sub>2</sub>O-Al<sub>2</sub>O<sub>3</sub>-TiO<sub>2</sub>-P<sub>2</sub>O<sub>5</sub>. *Solid State Ion* 96:195–200
6. Jackman SD, Cutler RA (2021) Effect of microcracking on ionic conductivity in LATP. *J Power Sources* 218:65–72
7. Soman S, Iwai Y, Kawamura J, Kulkarni A (2021) Crystalline phase content and ionic conductivity correlation in LATP glass-ceramic. *J Solid State Electrochem* 16:1761–1766
8. Kothari DH, Kanchan D (2016) Effect of doping of trivalent cations Ga<sup>3+</sup>, Sc<sup>3+</sup>, Y<sup>3+</sup> in Li<sub>1.3</sub>Al<sub>0.3</sub>Ti<sub>1.7</sub>(PO<sub>4</sub>)<sub>3</sub> (LATP) system on Li<sup>+</sup> ion conductivity. *Physica B: Condens Matter* 501:90–94
9. Duluard S, Paillassa A, Lenormand P et al (2017) Dense on porous solid LATP electrolyte system: Preparation and conductivity measurement. *J Am Ceram Soc* 100:141–149
10. Kotobuki M, Koishi M, Kato Y (2013) Preparation of Li<sub>1.5</sub>Al<sub>0.5</sub>Ti<sub>1.5</sub>(PO<sub>4</sub>)<sub>3</sub> solid electrolyte via a co-precipitation method. *Ionics* 19:1945–1948
11. Kotobuki M, Koishi M (2013) Preparation of Li<sub>1.5</sub>Al<sub>0.5</sub>Ti<sub>1.5</sub>(PO<sub>4</sub>)<sub>3</sub> solid electrolyte via a sol-gel route using various Al sources. *Ceram Int* 39:4645–4649

12. Bucharsky E, Schell K, Hintennach A, Hoffmann M (2015) Preparation and characterization of sol-gel derived high lithium ion conductive NZP-type ceramics  $\text{Li}_{1+x}\text{Al}_x\text{Ti}_{2-x}(\text{PO}_4)_3$ . *Solid State Ion* 274:77–82
13. Ma F, Zhao E, Zhu S et al (2016) Preparation and evaluation of high lithium ion conductivity  $\text{Li}_{1.3}\text{Al}_{0.3}\text{Ti}_{1.7}(\text{PO}_4)_3$  solid electrolyte obtained using a new solution method. *Solid State Ion* 295:7–12
14. Morimoto H, Awano H, Terashima J et al (2013) Preparation of lithium ion conducting solid electrolyte of NASICON-type  $\text{Li}_{1+x}\text{Al}_x\text{Ti}_{2-x}(\text{PO}_4)_3$  ( $x = 0.3$ ) obtained by using the mechanochemical method and its application as surface modification materials of  $\text{LiCoO}_2$  cathode for lithium cell. *J Power Sources* 240:636–643
15. Kim KM, Shin DO, Lee YG (2015) Effects of preparation conditions on the ionic conductivity of hydrothermally synthesized  $\text{Li}_{1+x}\text{Al}_x\text{Ti}_{2-x}(\text{PO}_4)_3$  solid electrolytes. *Electrochim Acta* 176:1364–1373
16. Deng Z, Wang Z, Chu IH, Luo J, Ong SP (2016) Elastic properties of alkali superionic conductor electrolytes from first principles calculations. *J Electrochem Soc* 163:A67
17. Nonemacher JF, Naqash S, Tietz F, Malzbender J (2019) Micromechanical assessment of Al/Y-substituted NASICON solid electrolytes. *Ceram Int* 45:21308–21314
18. Yan G, Yu S, Nonemacher JF et al (2019) Influence of sintering temperature on conductivity and mechanical behavior of the solid electrolyte LTP. *Ceram Int* 45:14697–14703
19. Cho YH, Wolfenstine J, Rangasamy E, Kim H, Choe H, Sakamoto J (2012) Mechanical properties of the solid Li-ion conducting electrolyte:  $\text{Li}_{0.33}\text{La}_{0.57}\text{TiO}_3$ . *J Mater Sci* 47:5970–5977
20. Gan Y, Malzbender J, Fu S et al (2021) Fracture behavior of solid electrolyte LTP material based on micro-pillar splitting method. *J European Ceram Soc* 41:5240–5247
21. Monroe C, Newman J (2005) The impact of elastic deformation on deposition kinetics at lithium/polymer interfaces. *J Electrochem Soc* 152:A396
22. Zhang M, Huang Z, Cheng J et al (2014) Solid state lithium ionic conducting thin film  $\text{Li}_{1.4}\text{Al}_{0.4}\text{Ge}_{1.6}(\text{PO}_4)_3$  prepared by tape casting. *J alloys compd* 590:147–152
23. Sebastiani M, Renzelli M, Battaini P, Bemporad E (2014) Focused Ion Beam and Nanomechanical Tests for High Resolution Surface Characterisation: New Resources for Platinum Group Metals Testing. *Platin Met Rev* 58:3–19
24. Sebastiani M, Johanns K, Herbert EG, Carassiti F, Pharr GM (2015) A novel pillar indentation splitting test for measuring fracture toughness of thin ceramic coatings. *Philos Mag* 95:1928–1945
25. Sebastiani M, Johanns K, Herbert EG, Pharr GM (2015) Measurement of fracture toughness by nanoindentation methods: Recent advances and future challenges. *Curr Opin Solid State Mater Sci* 19:324–333
26. Naqash S, Ma Q, Tietz F, Guillon O (2017)  $\text{Na}_3\text{Zr}_2(\text{SiO}_4)_2(\text{PO}_4)$  prepared by a solution-assisted solid state reaction. *Solid State Ion* 302:83–91
27. Dashjav E, Ma Q, Xu Q et al (2018) The influence of water on the electrical conductivity of aluminum-substituted lithium titanium phosphates. *Solid State Ion* 321:83–90

28. de Boer GB, de Weerd C, Thoenes D, Goossens HW (1987) Laser diffraction spectrometry: Fraunhofer diffraction versus Mie scattering. Part Part Syst Charact 4:14–19
29. Dashjav E, Gellert M, Yan G et al (2020) Microstructure, ionic conductivity and mechanical properties of tape-cast  $\text{Li}_{1.5}\text{Al}_{0.5}\text{Ti}_{1.5}\text{P}_3\text{O}_{12}$  electrolyte sheets. J European Ceram Soc 40:1975–1982
30. Yan G, Yu S, Yang W et al (2019) Anisotropy of the mechanical properties of  $\text{Li}_{1.3}\text{Al}_{0.3}\text{Ti}_{1.7}(\text{PO}_4)_3$  solid electrolyte material. J Power Sources 437:226940
31. Wang AN, Nonemacher JF, Yan G, Finsterbusch M, Malzbender J, Krüger M (2018) Mechanical properties of the solid electrolyte Al-substituted  $\text{Li}_7\text{La}_3\text{Zr}_2\text{O}_{12}$  (LLZO) by utilizing micro-pillar indentation splitting test. J European Ceram Soc 38:3201–3209
32. Schneider CA, Rasband WS, Eliceiri KW (2012) NIH Image to ImageJ: 25 years of image analysis. Nat Methods 9:671–675
33. Lauener CM, Petho L, Chen M, Xiao Y, Michler J, Wheeler JM (2018) Fracture of silicon: influence of rate, positioning accuracy, FIB machining, and elevated temperatures on toughness measured by pillar indentation splitting. Mater Des 142:340–349
34. Kojima H, Whiteway SG, Masson CR (1968) "Melting points of inorganic fluorides". Can J Chem 46:2968–2971
35. Wolfenstine J, Allen JL, Sakamoto J, Siegel DJ, Choe H (2018) Mechanical behavior of Li-ion-conducting crystalline oxide-based solid electrolytes: a brief review. Ionics 24:1271–1276
36. Wang JC (1984) Young's modulus of porous materials. J Mater Sci 19:801–808
37. Phani KK, Niyogi S (1987) Young's modulus of porous brittle solids. J Mater Sci 22:257–263
38. Fryxell R, Chandler B (1964) Creep, strength, expansion, and elastic moduli of sintered BeO as a function of grain size, porosity, and grain orientation. J Am Ceram Soc 47:283–291
39. Ramakrishnan N, Arunachalam V (1990) Effective elastic moduli of porous solids. J Mater Sci 25:3930–3937

## Figures

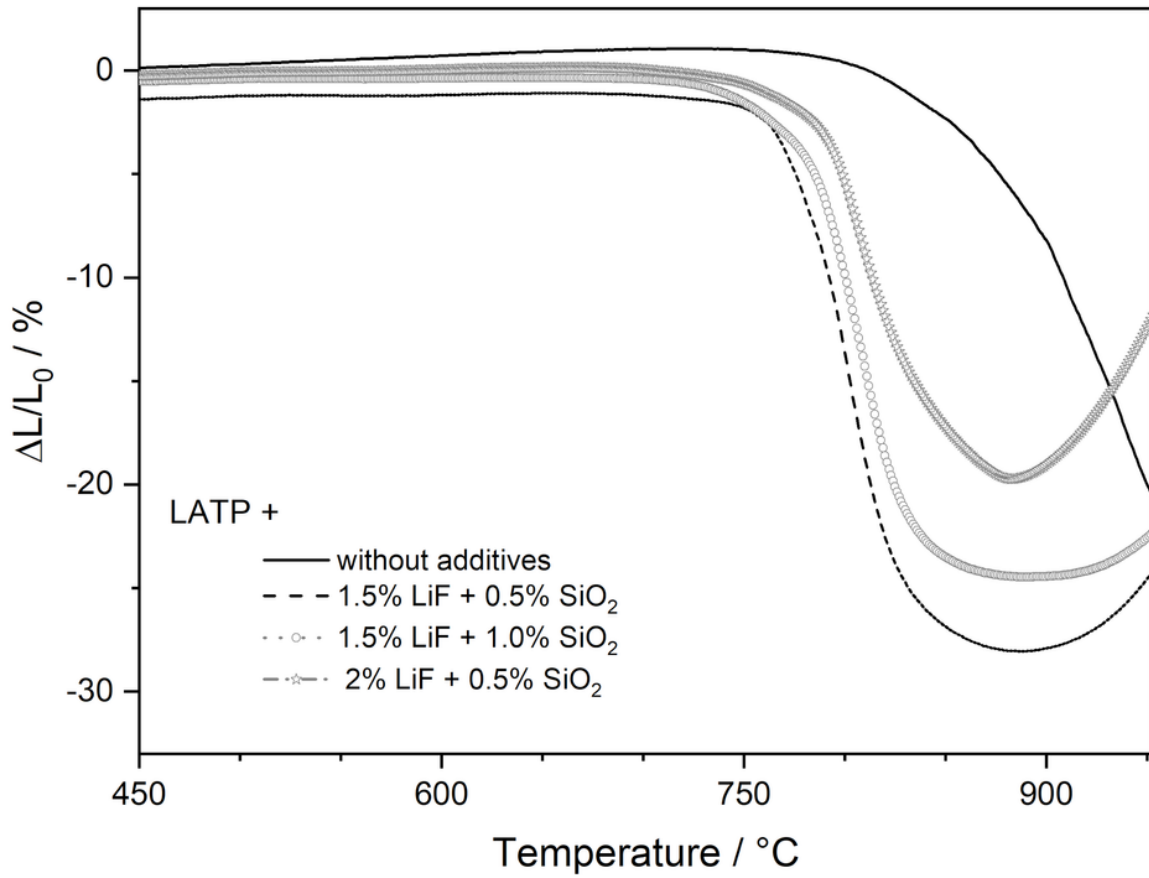


**Figure 1**

Length change of the different LAMP samples as a function of temperature determined by dilatometry. The shrinkage behavior is affected by the amount of sintering additives.

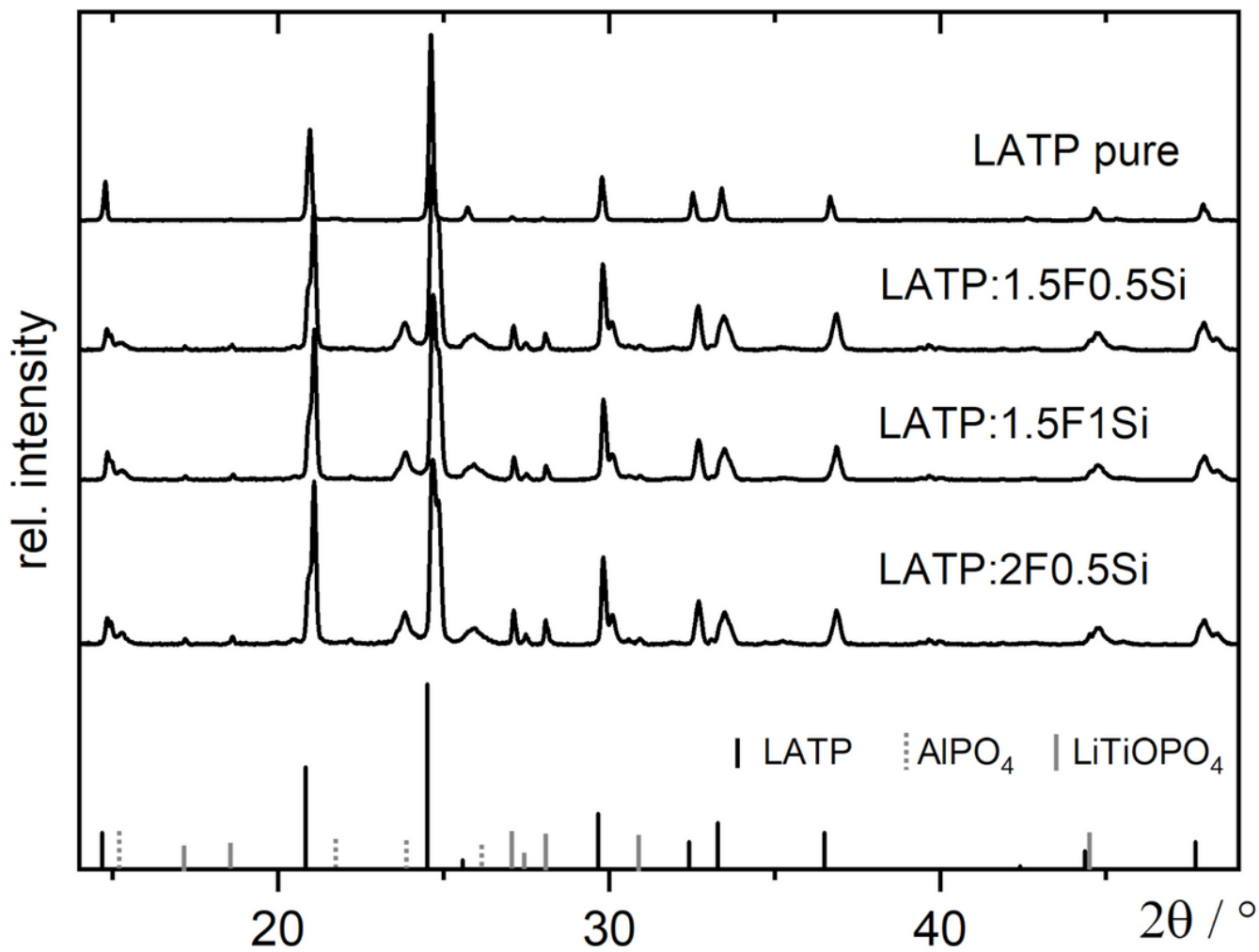


**Figure 2**

XRD patterns of the LATP samples with different amounts of additives. Secondary phases  $\text{LiTiOPO}_4$  and  $\text{AlPO}_4$  can be detected in small amounts.

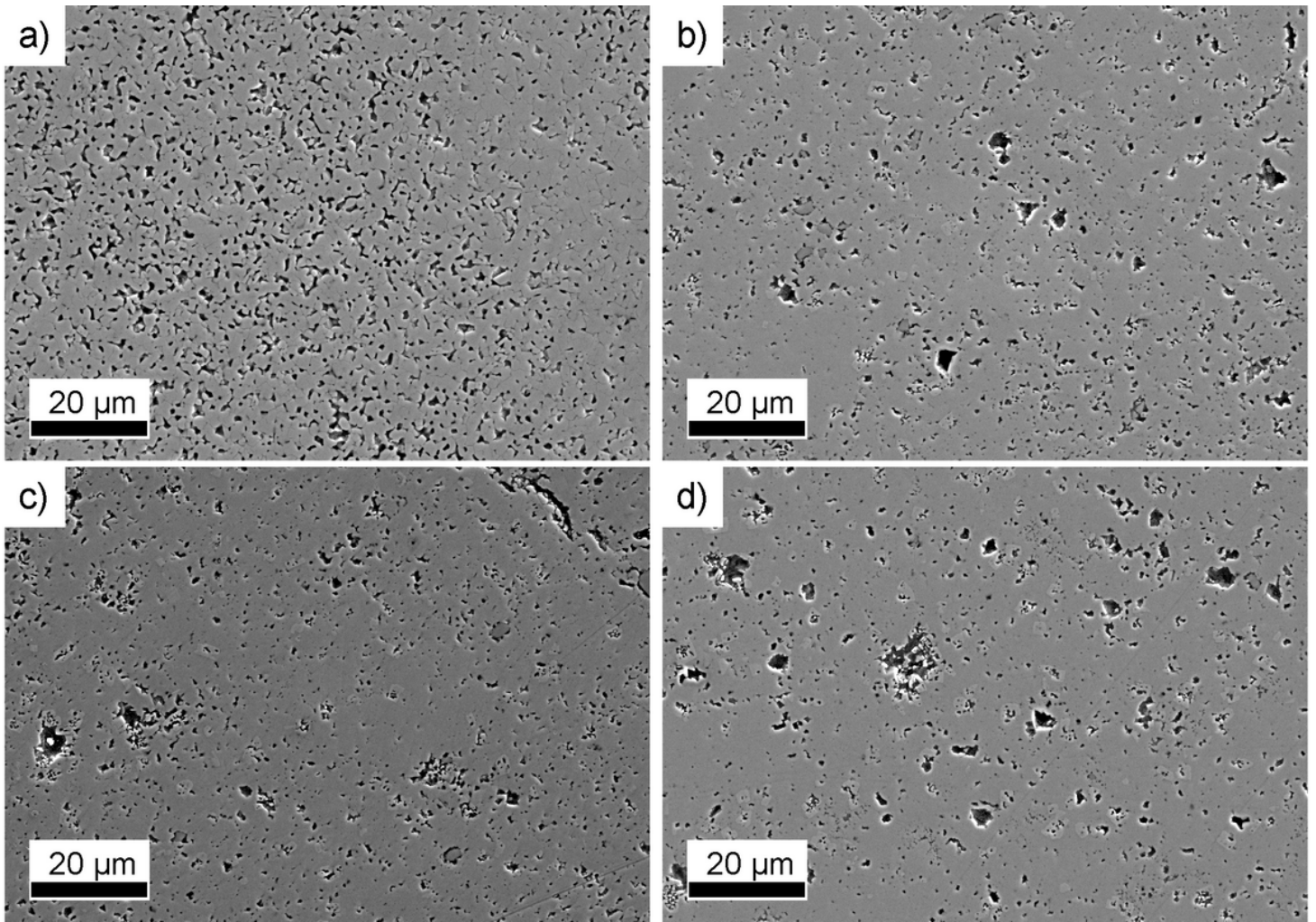


**Figure 3**

SEM images of a) LATP: pure, b) LATP:1.5F0.5Si, c) LATP:1.5F1Si, and d) LATP:2F0.5Si.

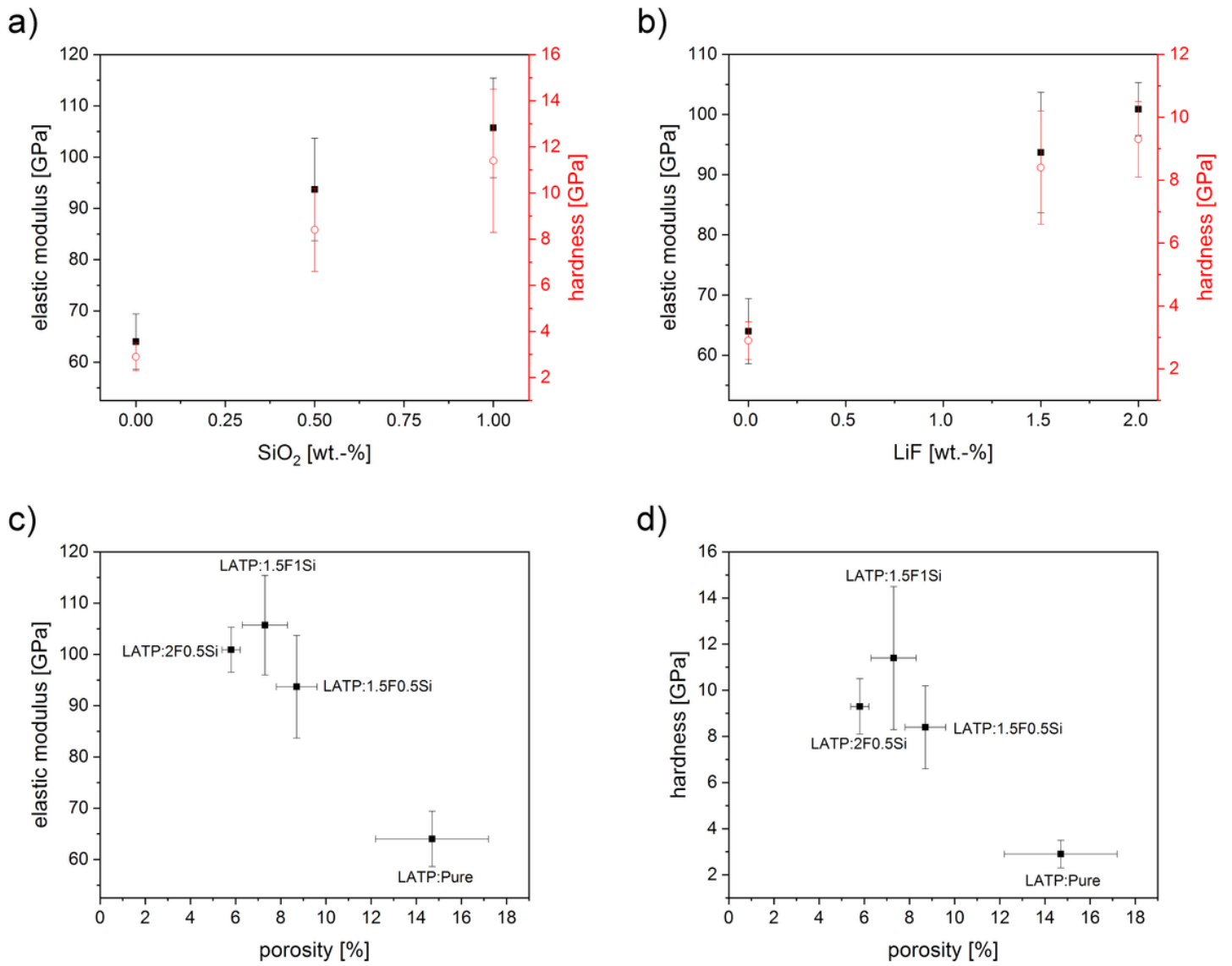


**Figure 4**

Elastic moduli (load of 30 mN) determined by indentation tests as a function of the (a) SiO<sub>2</sub> addition and (b) LiF addition. (c) Elastic modulus and (d) hardness values as a function of the porosity.

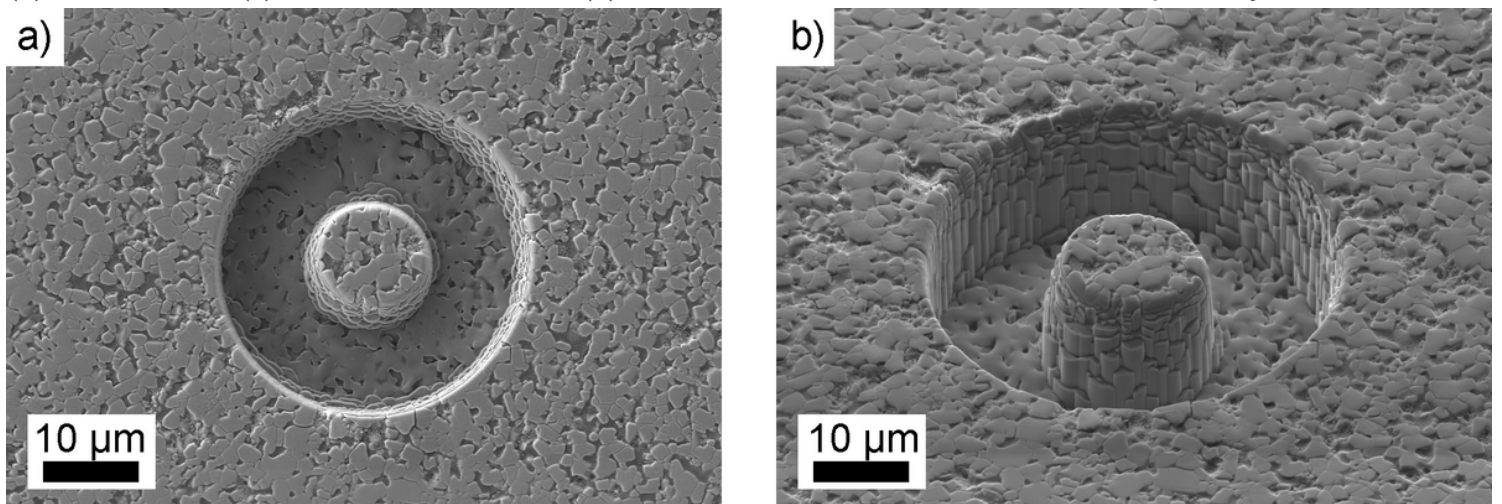


**Figure 5**

SEM micrographs of a 10  $\mu\text{m}$  pillar in LATP:1.5F1Si before testing, (a) top view and (b) side view (at 56° tilt angle).

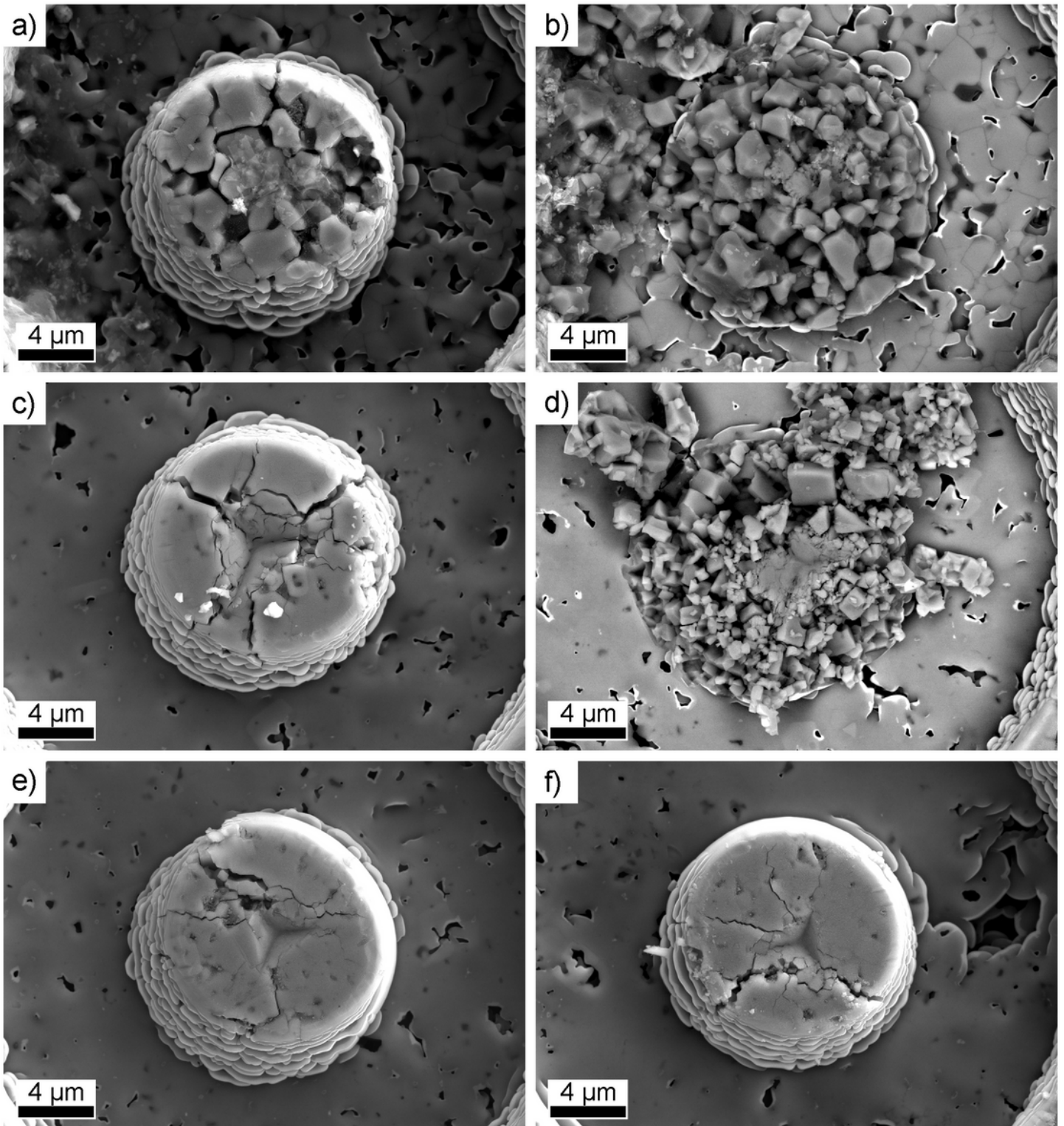


**Figure 6**

Representative images of micro-pillars after the indentation testing of the material LATP:Pure (a, b), LATP:1.5F0.5Si (c, d), LATP:1.5F1Si (e) and LATP:2F0.5Si (f).

## Supplementary Files

This is a list of supplementary files associated with this preprint. Click to download.

- [SupportingInformation.docx](#)